Experimental and Numerical Study of Swept Ramp Injection into a Supersonic Flowfield

James M. Donohue,* James C. McDaniel Jr.,† and Hossein Haj-Hariri‡
University of Virginia, Charlottesville, Virginia 22903

Time-averaged measurements of pressure, temperature, velocity, and injectant mole fraction are presented using the planar laser-induced iodine fluorescence technique in the complex three-dimensional compressible flowfield around a swept ramp fuel injector. Within the range of thermodynamic conditions present in the test case studied, the technique's accuracy is estimated to be 4% for pressure, temperature, and velocity and 3% for injectant mole fraction. Comparisons with numerical simulations using the SPARK three-dimensional Navier-Stokes computer code with an algebraic turbulence model are made at the centerplane of the flowfield as well as on three crossflow planes downstream of the injector. Calculations and measurements are in good agreement throughout the flowfield, with deviations on the order of 5%; however, in specific regions, such as in the base of the ramp, deviations are larger. A weak asymmetry in the incoming flowfield appears to be amplified by boundary-layer separation occurring when the ramp-generated shock reflects off the tunnel walls. Ramp-generated vortices are weaker in the calculated results due to the effects of numerical viscosity in the vortex cores. This leads to less turning and mixing of the jet plume than observed in the experiments. The rate of decay of the maximum injectant mole fraction with streamwise distance is greater for the present ramp injection scheme than for previously measured transverse injection schemes. In the recirculation region at the base of the injector, laminar calculations show better agreement with the measurements than turbulent calculations.

Introduction

S CRAMJET propulsion systems rely on injection and burning of fuel in very high speed flowfields. In such an environment the fuel remains inside the combustion chamber for such short durations that rapid mixing of the fuel into the freestream air is essential for an acceptable design. The swept ramp fuel injector design studied here enhances mixing greatly and is a generic configuration under investigation for scramjet combustors. A number of experimental and numerical studies on the ramp injector geometry have been reported previously.[1-3]

The process of designing high-speed propulsion systems is relying more and more heavily on computational fluid dynamics (CFD) simulations for predicting the complex compressible flowfields that arise. The SPARK three-dimensional CFD code has been used for the calculation of the internal flow in scramjet combustors.[4] Bench mark data sets are needed for validation of any CFD code. A detailed comparison of the SPARK calculation to an extensive data set in the Mach 2 flow over a step with staged transverse injection has recently been accomplished as an important step in the validation of the code.[5] The validation data set was obtained using a nonintrusive optical technique, planar laser-induced iodine fluorescence (PLIIF). Optical measurement techniques become a necessity in high-speed flows where introduction of a measurement probe into the flow can alter the flowfield drastically. The PLIIF technique, also used in the current work, has evolved from a method for qualitative flow visualization[6] to a quantitative single-point measurement technique of multiple parameters,[7] to a planar multiple-parameter measurement technique.[8-10]

The purpose of this investigation is to conduct a detailed study of the complex three-dimensional flowfield generated by the swept ramp injector configuration using the advanced experimental and computational tools now available. Emphasis is placed on the generation of a quantitative data set containing several planes of data that can be used to evaluate code performance. Comparisons of the data to both turbulent and laminar calculations are made to address the effect of turbulence modeling.

Experimental Approach

Test Facility

Experiments are carried out in a continuous-flow Mach 2 wind-tunnel facility specifically designed to allow for iodine seeding and to resist iodine corrosion. Seeding with molecular iodine, rather than particle seeding, as used in many other measurement techniques, has the great advantage of tracking the flow accurately through shock waves and regions of high gradients.[7] A two-dimensional Laval nozzle exits into the test section shown schematically in Fig. 1. The freestream stagnation pressure and temperature are 1960 Torr and 300 K, respectively. The incoming stagnation conditions are held constant to within 1% during the test. The rectangular test section contains fused silica walls on three sides for optical access to the flowfield. The fourth wall contains the swept ramp injector. The tunnel height remains constant until 8.5 ramp heights downstream of the injector where the injector wall is diverged at a 2.7-deg angle. Air is injected from the base of the ramp, parallel to the ramp top surface, from a circular injection orifice contoured to give Mach 1.7 flow at the injector exit. The injector stagnation pressure and temperature are 1860 Torr and 300 K, respectively.

PLIIF Measurement Technique

To conduct the PLIIF measurements, the iodine-seeded air is probed with the 514.5-nm line of a high-power argon-ion laser. The laser beam is spread into a 200-μ-thick sheet to illuminate the plane of the flowfield being measured. Images of the resulting fluorescence are collected with a liquid-nitrogen-cooled charge-coupled device array camera with 516×516 pixels and 14-bit digitization. Exposure times are on the order of 10 s, and so all results are time averaged. For

*Graduate Research Assistant, Department of Mechanical, Aerospace, and Nuclear Engineering. Member AIAA.

†Associate Professor, Department of Mechanical, Aerospace, and Nuclear Engineering. Member AIAA.

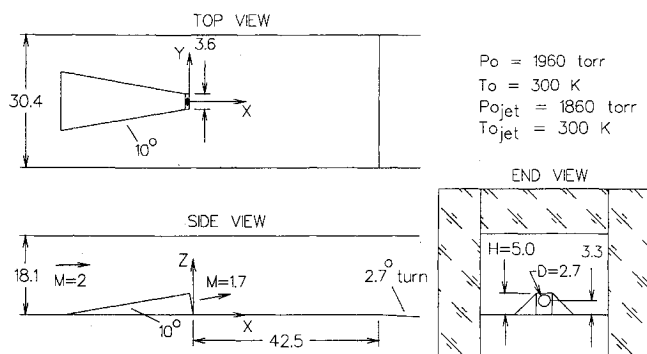‡Assistant Professor, Department of Mechanical, Aerospace, and Nuclear Engineering. Member AIAA.

Fig. 1 Test section geometry and operating conditions (dimensions shown in millimeters).

velocity, pressure, and temperature measurements, the laser is operated with an intracavity etalon to produce single-frequency, narrowband output of about 1.5 W. The laser is tuned in frequency so that an iodine absorption spectrum can be measured. A background image, taken with no iodine seeded into the air, is subtracted from all of the images collected.

The PLIIF measurement technique, presented in detail previously,[7,8] is based on a model that predicts the iodine fluorescence signal as a function of laser frequency. The model used here accounts for 133 iodine absorption lines located within a 200-GHz region centered on the argon laser gain profile. The collected signal is a complicated function of the pressure P, temperature T, and frequency of the laser ν, but is proportional to the laser intensity I and to the number density of iodine present in the flow N_{I_2}:

$$S_f = C \, I \, N_{I_2} f(P, T, \nu) \qquad (1)$$

The constant C includes factors such as collection efficiency and molecular parameters. The fact that the signal level is directly proportional to iodine number density will be utilized for injectant mole fraction measurements. The modeled thermodynamic dependence of the signal is used to determine the pressure and temperature. The Doppler frequency shift of the fluorescence spectrum is used to determine velocity.

For the measurement of injectant mole fraction, the ratio of two images, collected at a fixed laser frequency, is used. In one image, iodine is seeded only in the injector air; in the other, iodine is seeded everywhere in the flowfield. Since the change in seeding conditions does not affect the local thermodynamic conditions, the complex function f cancels in the ratioed image, and the resulting signal ratio is proportional to the ratio of the injectant to total number densities or the injectant mole fraction.[11] The concentration of iodine in the seeded air will be different for the two flowfield seeding cases because the flow rate of air through the seeding chamber is very different for the two cases. This results in a signal ratio different from unity in the injector core; however, since the injectant mole fraction must be 100% in this region, the ratioed image is scaled properly to give the distribution of injectant mole fraction in the measurement plane.

To determine the distribution of pressure, temperature, and velocity, a fluorescence spectrum at each position in the laser sheet is measured. PLIIF images are collected at discrete frequencies over the desired spectral region. At each point in the image a spectrum is constructed and normalized using the peak signal level. Figure 2 illustrates the strong thermodynamic dependence of the shape of the spectrum, showing two representative absorption spectra calculated at different pressures and temperatures. The left peak in the curves corresponds to the P48 (44, 0), P103 (49, 0) transition pair in the iodine absorption spectrum, and the right peak corresponds to the P13 (43, 0), R15 (43, 0) transition pair.

Two parameters, T_{ratio}, the ratio of the left to right peaks, and P_{ratio}, the ratio of the valley between the two peaks to the

right peak, are used to characterize the shape of the spectrum and to determine the pressure and temperature. The ratio of the two peak heights, T_{ratio}, is strongly temperature sensitive due to the different Boltzmann population fractions of the two transition pairs, and P_{ratio} is sensitive to pressure due to collisional broadening. Primarily because the transition pairs used here are not well separated in frequency, these two ratio parameters are functions of both pressure and temperature; however, for each (P_{ratio}, T_{ratio}) pair there corresponds a unique (P, T) pair. The fluorescence model is used to define this mapping between (P_{ratio}, T_{ratio}) and (P, T).[12]

The velocity is determined by measuring the frequency shift of the measured spectrum in the flowfield relative to an unshifted spectrum measured in a low-pressure static cell. The frequency shift in the spectrum is due to 1) a Doppler shift, because flowfield molecules have a velocity component in the direction of the laser sheet, and 2) the collisional impact shift, which is a known function of pressure and temperature.[7,8] After the subtraction of the impact shift, calculated from the previously measured pressure and temperature, the remaining Doppler shift gives the velocity component in the direction of the laser sheet. A second set of measurements with a different laser sheet direction is needed to determine the two components of velocity in the plane.

The uncertainty expected in the measurements has been discussed in detail previously,[7,8] although it should be emphasized that the uncertainties are strong functions of the conditions being measured. At high pressures (around 600 Torr, depending on the temperature), the transition lines broaden so much that the double peak shape of the spectrum is lost and the measurement method breaks down. Velocity measurements rely on a Doppler shift, and so when the flowfield velocity becomes excessively small, errors in determining the spectrum frequency shift increase. Higher pressure conditions lead to a broader spectrum and increase the error in determining the spectral shift and the velocity. At low pressure (and high temperatures) the velocity error is estimated to be about ±20 m/s. Estimated uncertainties for the range of flowfield conditions in the present test case are 4% for pressure, temperature, and velocity and 3% for injectant mole fraction. Close to walls the errors will be larger due to higher background image levels resulting from light scattering from the surfaces and fluorescence from iodine deposited on the walls.

A large amount of data must be acquired, stored, and processed using the PLIIF technique. About 70 images are required to produce fluorescence spectra with reasonable resolution. Each of these images contain about 1/2 Mbyte of data. Two such data sets are required to recover both velocity components; therefore, about 70 Mbytes of raw data must be acquired for each plane studied. The image files are transferred automatically to an IBM RS6000 workstation to store and process the data efficiently.

Numerical Approach

The three-dimensional version of the SPARK family of Navier-Stokes solvers, originally developed by Drummond[13]
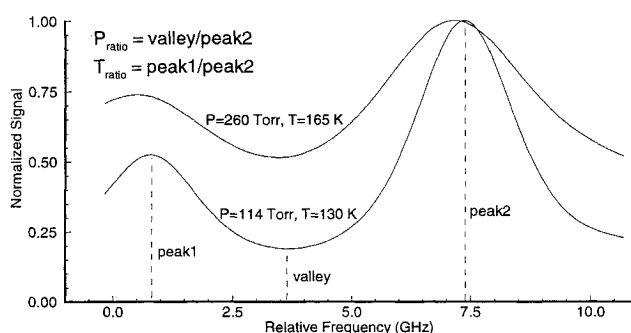

Fig. 2 Thermodynamic dependence of the iodine fluorescence spectrum.

at NASA Langley, is used to compute the flowfield. Many studies have been made using SPARK, and experimental validation for certain flow configurations is now documented.[5] The program uses fourth-order compact differences to approximate the derivatives.[14] The algorithm used to integrate the equations is based on a MacCormack predictor-corrector scheme. Wall turbulence is modeled using a Baldwin-Lomax scheme along the no-slip boundaries. A mixing length model similar to that used by Eklund and Northam[15] is adopted to model the jet turbulence. In the present model the mixing length used at each crossflow plane is based on the typical spatial separation between the 5% of maximum concentration contour and 95% of maximum concentration contour occurring on that crossflow plane. A smooth transition in mixing length is imposed at the boundaries between the jet region and the region outside the jet. A pseudotransient scheme using local time stepping is used and greatly accelerates the convergence to the desired steady-state solution. The program has the ability to simulate chemical reactions, a feature that is turned off in the present study.

Grids are generated to fit all solid boundaries smoothly and are compressed at the location of boundary layers and shear layers (typical minimum grid spacing in these regions is 70 μ). The ramp region and the mixing region (beginning at the downstream end of the ramp) are calculated using two separate grids to provide for the different grid spacings needed in the two regions. Approximately 100,000 grid points are used in each region. This is a relatively small number of points compared with what would normally be used for such a complex three-dimensional flowfield, but the size was limited by the computational resources available. The outflow conditions from the ramp region are interpolated onto the inflow grid of the mixing region and used as inflow boundary conditions. The flowfield is supersonic, except in the thin boundary layers, and so no perceptible upstream influence is expected.

At the inflow boundary of the ramp region, velocity, pressure, temperature, and concentration are specified by a SPARK two-dimensional calculation of the nozzle flow. This calculation was started from a plug flow at the throat of the nozzle with conditions assuming choked isentropic flow from the measured stagnation conditions, as in Eklund et al.[5] The bottom wall, top wall, and ramp surfaces are treated as no-slip surfaces. Zeroth-order extrapolation is used to ensure vanishing of the pressure, temperature, and concentration gradients at these surfaces. The sidewalls are treated with slip conditions so zeroth-order extrapolation is again used to impose zero gradients in all flow parameters, except the lateral velocity, which is set to zero. At the outflow boundary, first-order extrapolation for all parameters is used, since the flow is supersonic (except in thin boundary layers).
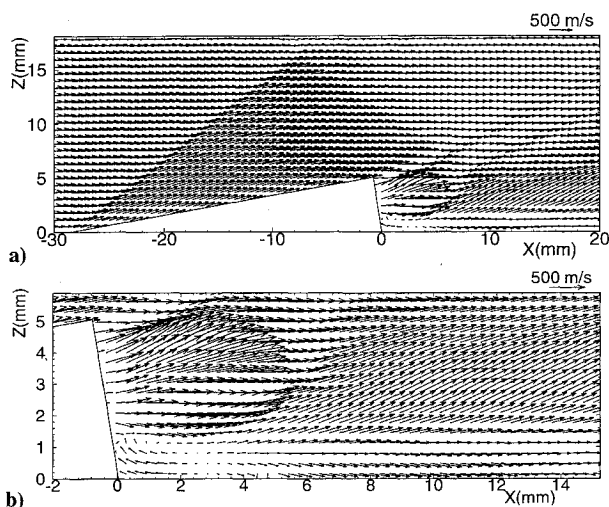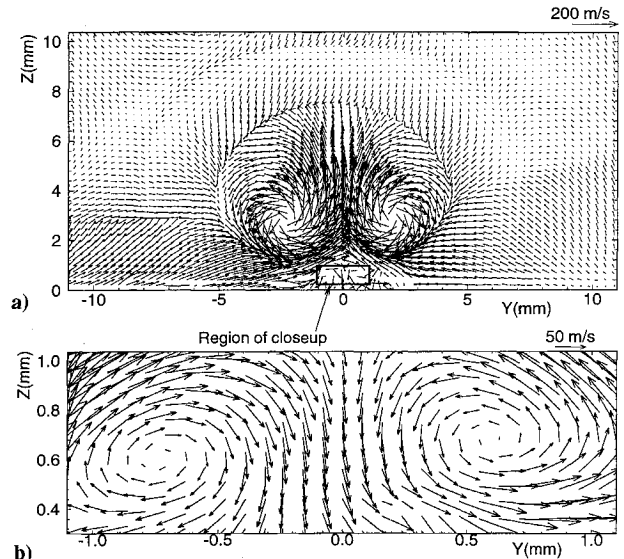

Fig. 4 a) Measured crossflow velocities at $X/H = 2$ and b) closeup of secondary vortices.

Results and Discussion

The basic features of the investigated flowfield can be illustrated using the measured velocity distributions shown in Figs. 3 and 4. The freestream air enters the test section at Mach 2 and passes over the ramp. A shock is generated at the leading edge of the ramp when the flow is turned parallel to the ramp's top surface (see Fig. 3a). This ramp shock is reflected from the opposite wall of the wind tunnel and passes downstream of the injector. The pressure at the jet exit plane is greater than the ramp base pressure, and so an underexpanded jet is formed. Figure 3b shows a closeup of the jet region. The flow over the top surface of the ramp is deflected downward through an expansion fan as it turns the corner at the end of the ramp. A shock is formed when this freestream air interacts with the jet and is turned back. A conical-shaped shock emanates from the region in the underexpanded jet where the barrel shock intersects the Mach disk (referred to as the "triple point" when the jet is viewed in cross section). The recirculation region in the ramp base below the jet, which is advantageous for flame holding in the combusting flow, can be seen clearly in Fig. 3b.

The ramp generates streamwise vortices when high-pressure air on top of the ramp is forced over the edges and into the low-pressure air in the expansion regions on either side of the ramp. The vortices are convected downstream past the jet, mixing freestream air into the jet plume and carrying it away from the wall. These strong counter-rotating vortices are seen in the measured crossflow plane velocity vectors shown in Fig. 4a. Asymmetry seen in the velocity field appears to be caused by an asymmetric reflection of the ramp shock. (The cause of this asymmetry is addressed later in the discussion of the crossflow pressure distributions.) The effect of the conical shock that was generated at the triple point can be seen by the abrupt turning of the velocity vectors along a circular border surrounding the vortices. Evidence of the curved shock formed by freestream air turning around the end of the ramp and interacting with the jet, as discussed earlier and subsequently referred to as the freestream/jet-interaction shock, is seen along a larger circular border. Figure 4b shows a closeup of the two smaller secondary vortices generated very close to the wall. These secondary vortices are difficult to see in Fig. 4a where only every fourth measured vector is displayed. Figure 4b demonstrates that measurement spatial resolution is extremely high, with a measurement grid spacing of about 60 μ for the crossflow planes and 120 μ for the centerplane data.

Centerplane Results

Results are presented for a plane taken through the center of the test section normal to the bottom wall. It is important to

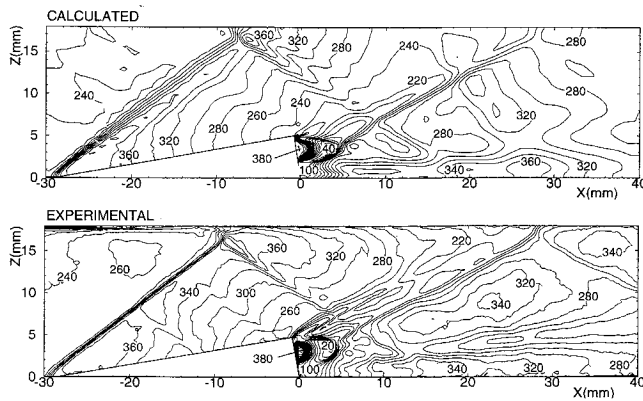Fig. 3 a) Measured centerplane velocity distribution and b) closeup of jet region.

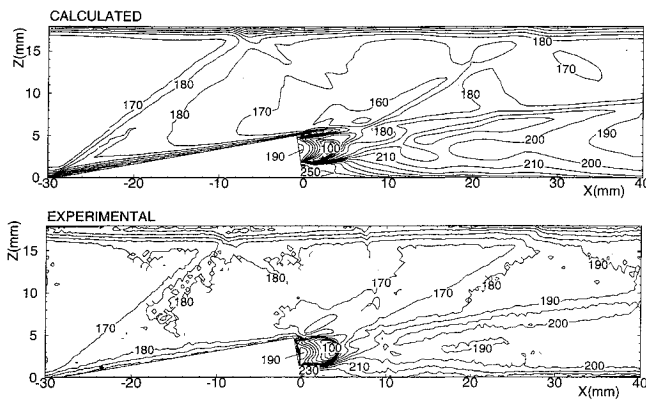Fig. 5 Centerplane pressure distribution, Torr.

Fig. 6 Centerplane temperature distribution, K.

emphasize that this is not a slice through a two-dimensional flowfield and that three-dimensional effects are significant in understanding the results that follow. For comparison, both experimental and numerical results are shown in each of the remaining figures.

The centerplane pressure distribution is presented in Fig. 5. Agreement between the experiment and numerical results is generally very good, with differences mostly confined to specific regions. Shocks are captured with varying resolution in the calculation depending on the grid refinement in any particular region. The thickness of the ramp shock in the experiment is very narrow; however, in the calculation, where the grid is relatively coarse in the freestream, the shock is quite wide and exhibits a region of pressure overshoot just downstream of the shock. The angle of the ramp shock is initially the same in the experiment and in the calculation, but near the top wall a slight curvature of the shock is seen in the calculation. The calculation predicts reasonably well the complex reflection caused by the shock-wave/boundary-layer interaction when the ramp shock reflects off the top wall. The experiment shows an effective reflection point located further from the wall and a steeper reflected shock that crosses the injection jet further upstream than in the calculations. Sidewall boundary layers, which were not modeled here, could have an important effect on the reflected shock strength and structure. Two weak compression waves are seen in the experimental results to pass through the ramp shock toward the ramp top surface and are caused by a slight imperfection in the nozzle design.

The measured and calculated pressure distributions in the region near the jet agree quite well, with differences, such as shock resolution, due mostly to the lack of grid resolution. Pressures in the recirculation region in the ramp base match well, whereas in the very low pressure jet core just before the Mach disk a slightly lower pressure is seen in the measurement. The distance from the jet exit to the Mach disk agrees

well, although the width of the barrel shock is greater in the experiment. The freestream/jet-interaction shock is not captured in the calculation because the jet does not expand sufficiently to interact strongly with the freestream flow. The conical shock leaving the jet triple point is seen to reflect more weakly off the top surface in the calculation than in the experiment. This is again due to grid resolution, as the grid spacing is increased in the downstream direction to reduce calculation time. Notice that along the top wall experimental pressure contours turn parallel to the wall, indicating strong pressure gradients normal to a solid surface. This unphysical result is caused by errors due to high background signal levels close to walls, as discussed earlier.

Temperature results are shown in Fig. 6. The main features expected are present in both experiment and calculation. Boundary layers in both cases are of similar thickness, and both exhibit the thickening that occurs at shock reflections. Again, agreement is good for the length of the underexpanded jet, but the experiment shows the jet expanding more than the calculation. In the ramp base recirculation region temperatures are about 10% higher in the calculation than in the experiment. In a laminar calculation the temperature in this region was more in agreement with the measurement, a point that will be discussed further in a later section.

Contours of the streamwise component of velocity are plotted in Fig. 7. Agreement is excellent at the inlet to the test section where the velocity is known with confidence from isentropic relations, simple nozzle calculations, and from laser-Doppler-velocimetry measurements made previously.[5] This agreement also verifies the accuracy of the empirical constant used in the impact shift relationship as measured by Hartfield.[8] A sudden increase in velocity, followed by a rapid decrease, is observed experimentally across the freestream/jet-interaction shock and the conical triple point shock. This can be expected because of their highly curved shape, giving a three-dimensional relieving effect typical of the flow through a conical shock. Velocity near the jet exit shows the poorest agreement. The jet exit velocity is set as a boundary condition for the calculation assuming isentropic flow to Mach 1.7 from the measured stagnation conditions. The discrepancy at the jet exit is especially unclear considering that the measured pressure and temperature are in very good agreement with the assumed isentropic values. The region close to the ramp surface just downstream of the ramp shock has flowfield conditions similar to those expected at the jet exit, and agreement between the measurement and calculation in this region is reasonable. This suggests that the fluorescence model is not the cause of the discrepancy. The reverse flow velocities in the recirculation zone are also significantly different in the experiment and calculation. Errors in the measured velocities at the jet exit and in the ramp base may be due to laser sheet reflection from the ramp and wall surfaces. Calculated velocities in the recirculation zone may be sensitive to many factors such as grid spacing, boundary conditions, and turbulence modeling.
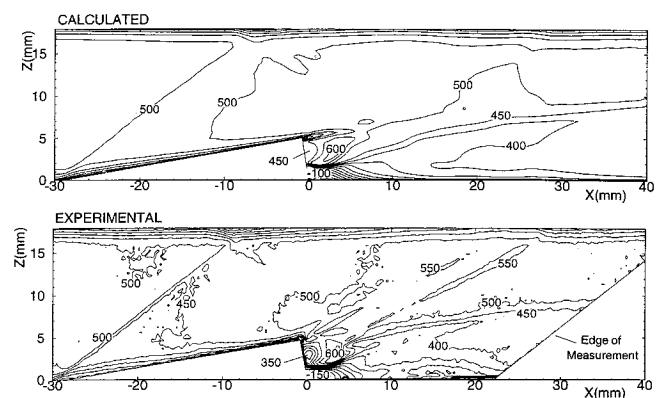

Fig. 7 Centerplane streamwise velocity distribution, m/s.

The centerplane injectant mole fraction χ distribution is presented in Fig. 8. Comparison shows that the penetration of the jet plume into the freestream is in good agreement; however, mixing of the experimental plume occurs more rapidly. This rapid mixing is the result of the stronger vortices in the experimental flowfield and will be discussed further in the next section.

To give a clearer quantitative comparison of experimental and calculated results, two sets of profiles are extracted from the centerplane results and given in Figs. 9 and 10. Figure 9 gives profiles across the inlet to the test section just upstream of the leading edge of the ramp (at $X = -31$ mm and $Y = 0$). Measured and calculated pressure, temperature, and streamwise velocity results are all in excellent agreement. Figure 10 gives profiles across the test section at a location half a ramp height downstream of the injector, cutting through the injector core (at $X = 2.5$ mm and $Y = 0$). Comparison between measured and calculated results shows clearly the differences seen in the centerplane contour plots. The freestream/jet-interaction shock is missing in the calculations but is apparent in the experimental results as a sudden increase in conditions at around $Z = 6$ mm. Calculated temperatures are again seen to be higher than measured in the recirculation region below the jet. Care should be taken when making point-by-point comparisons, such as these, in a complex three-dimensional flowfield with many flow features. Large differences at a point may be due more to the movement of a flow structure than a difference in the flow quantities in that structure (e.g., a small change in a shock angle can change greatly the location of its reflections downstream).

Crossflow Plane Results

Measurements were made in three crossflow planes that reveal many of the three-dimensional features of the flowfield. A measurement over the entire cross section of the tunnel was not possible due to optical access limitations. The results shown here are contained in an area 15 mm high × 20 mm wide, compared with the full tunnel cross section of about
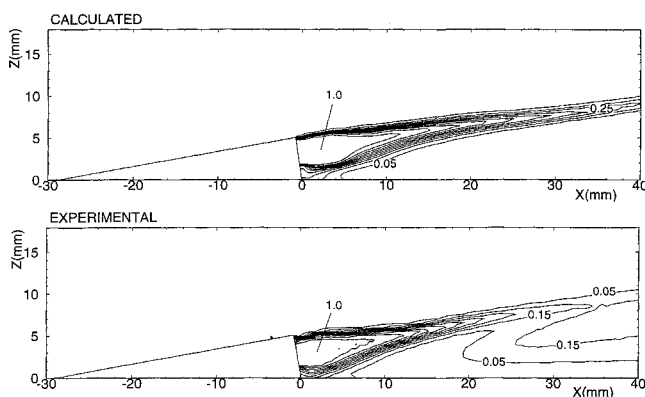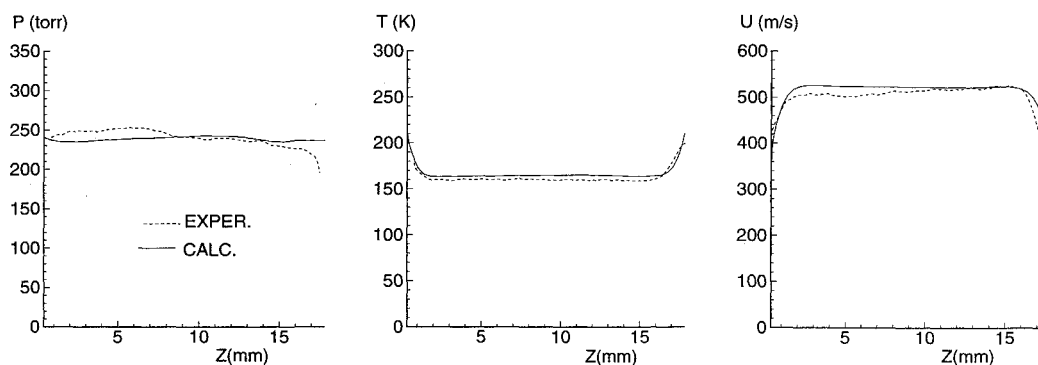
18 × 30 mm. The first plane is located in the near field of the ramp at half a ramp height, or 2.5 mm, downstream of the ramp face and cuts through the core of the underexpanded jet. The second plane, taken at a location 2 ramp heights, or 10 mm, from the ramp, shows where the vortices begin to interact strongly with the jet. The last plane is at 8 ramp heights, or 40 mm, from the ramp where turbulent mixing should be dominant.

Velocity vectors at the three crossflow planes are shown in Fig. 11. At the first plane the jet is seen expanding outward, whereas the ramp-generated vortices wrap around it. The vortices are stronger in the measurement, as seen most clearly in the larger velocity vectors beneath the jet core. The reflected ramp shock is noticeable in the measurement just above the jet region, at about 8 mm above the bottom wall, where the experimental vectors turn suddenly along a line. In the calculation, the ramp shock, barely visible at about $Z = 10$ mm, is located farther above the jet, as was seen earlier in the centerplane results. The second plane at $X/H = 2$ shows that the ramp shock has passed partially through the jet/vortex region and is highly asymmetric in the experimental flowfield. Concentric rings around the vortex region in the measurement show the expansion fan that originates at the ramp tip, the freestream/jet-interaction shock, and the strong conical shock from the Mach disk triple point. These features are weaker, or not observed, in the calculation, due in part to the lack of grid resolution. The core of the vortices, at $X/H = 2$, again show larger velocities in the experiment than in the calculation. At $X/H = 8$ the asymmetry in the measured flowfield is more pronounced. The important feature to notice is that the vortices remain strong at this downstream location and are still affecting the mixing considerably. The strong upward velocities, measured between the vortices, carry the injectant plume and the vortex cores away from the wall. The experimental results show more upflow and lifting of the vortices than the calculation.

Figure 12 shows pressure contours in the three crossflow planes. The flowfield features, such as shock locations and the position and strength of the vortices as discussed earlier, are also apparent in the pressure field. Shocks are smeared in the calculation and the vortices are weaker, evidenced by the much higher pressure gradients in the measured vortex cores. The action of artificial viscosity (which is related to grid resolution) is a significant cause of shock smearing and is the most probable cause of the strong vortex damping seen. Artificial viscosity is particularly high in vortical flow regions because flow lines often move tangentially to, rather than normally into, grid elements. Using many more grid points (which was impractical for this study because of limited computational resources) or using an adaptive grid where grid points are relocated into high-gradient locations such as these (a formidable task for this highly complex three-dimensional flow) would help decrease these effects. The experiments show good symmetry until the ramp shock passes through the jet and vortices. Shocks coming from the upper corners of the rectangular channel and following the reflected ramp shock
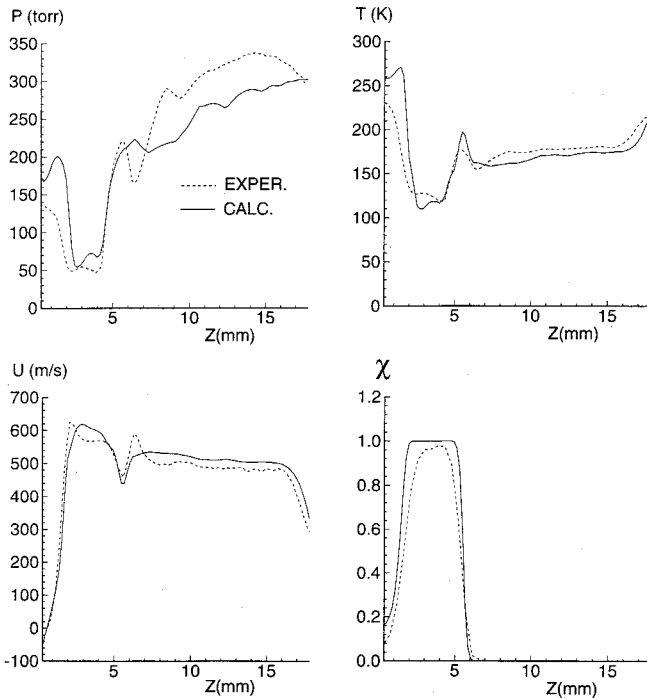

Fig. 8   Centerplane injectant mole fraction distribution.

Fig. 9   Profiles across the inlet to the test section at $X = -31$ mm and $Y = 0$.

Fig. 10 Profiles across the test section cutting through the jet core at X = 2.5 mm and Y = 0.

Temperature distributions in the crossflow planes are shown in Fig. 13. The same features seen in the pressure fields are seen here as well. A significant difference between the experiment and the calculation is the higher temperature in the recirculation region below the jet in the first plane. The measured flowfield symmetry is again apparent until the ramp shock passes, as seen in the X/H = 2 plane measurement. Notice the action of the vortices on the bottom wall boundary layers, thinning them directly below the vortex. The warmer air in the boundary layer is carried upward into the plume
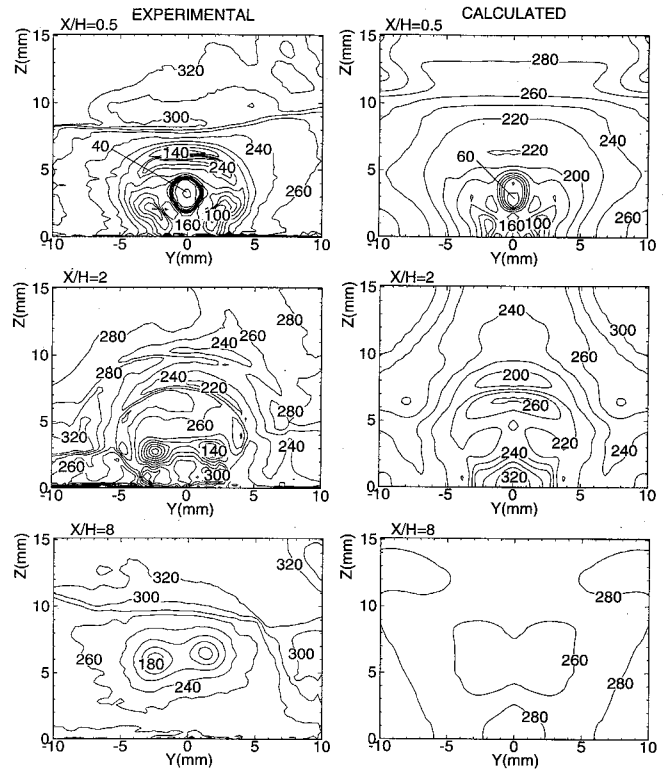

Fig. 11 Crossflow velocity distributions.

Fig. 12 Crossflow plane pressure distributions, Torr.

are seen in the X/H = 2 plane. These shocks are caused as the curved ramp shock reflects from the corners of the channel. Since the shock-wave/boundary-layer interaction at the top wall is strong (as seen in the centerplane results), it can be expected that separation would occur at the corners and on the side walls. Since separation zones can be very sensitive to small changes in shock angles, it is possible that a weak asymmetry in the incoming flowfield is amplified by the shock-induced separated regions. Modeling the sidewalls correctly with no-slip conditions should be incorporated into the calculations to study this effect.
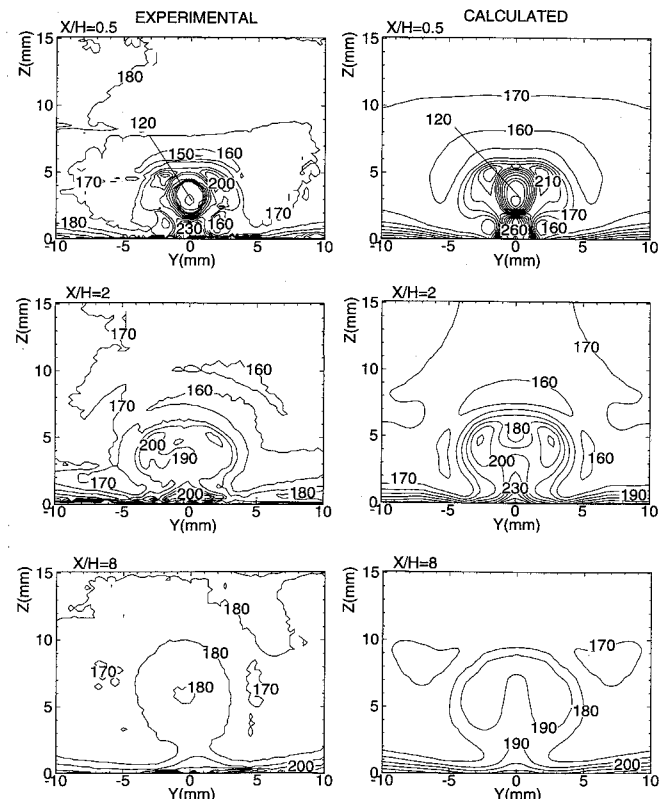

Fig. 13 Crossflow plane temperature distributions, K.

region, as seen in the $X/H = 8$ plane results. Notice that the plume shape at $X/H = 8$ is different for the calculated and experimental results due to the weaker calculated vortices.

The injectant mole fraction χ crossflow distributions are shown in Fig. 14. The near-field results show close agreement, but at the planes downstream the effect of the weaker ramp-generated vortices predicted in the calculation becomes apparent. In the $X/H = 2$ plane the action of the vortices is to spread the plume laterally more than in the calculation. Far downstream the plume is more uniformly mixed with the freestream air in the experiment than in the calculation, approaching a circular shape where the turbulent diffusion begins to dominate. The kidney-shaped structure is still present in the calculation at $X/H = 8$, whereas in the experiment the lobes have merged along the plume centerplane, giving the distribution seen earlier in the centerplane injectant mole fraction results (see Fig. 8).

To give a more global view of the degree of mixing produced by the ramp injector studied, a plot showing the decay of the maximum injectant mole fraction χ_{max} in the downstream direction is shown in Fig. 15. The maximum mole fraction occurring in a crossflow plane is displayed on a log-
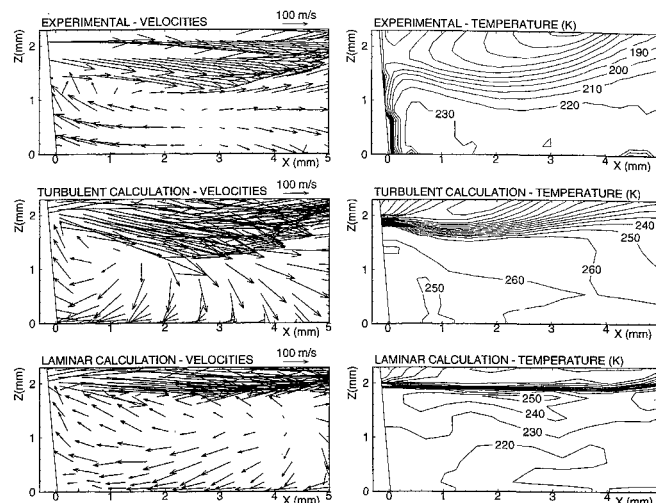
Fig. 16 Effect of turbulence model in recirculation region.

log plot vs X/D (where D is the throat diameter of the injector orifice) for both the experimental and calculated results. Agreement is within about 10% over the range studied. The experimental values downstream of approximately $X/D = 10$ follow a power law decay with an exponent of -1.3. This decay exponent is significantly larger than the value of -0.8 found in transverse injection cases.[16] In the present ramp injector case the vortices remain strong and dominate the mixing process over the range of X/D presented. In the transverse injection case, the streamwise vortices formed are weaker, and their effect decreases more quickly, resulting in a decrease in the mixing rate. Although the actual mixing occurs through turbulent diffusion, the vortices facilitate this process by greatly increasing the injectant/freestream interface and, therefore, directly increase the resulting mixing rate.

Turbulence Modeling Effects

To investigate the effects of turbulence modeling, a laminar calculation was also performed and compared with the turbulent results. Aside from the expected result of reduced mixing in the plume at $X/H = 8$ due to the lack of turbulent diffusion, the only significant difference between the turbulent and laminar results was seen in the recirculation region in the base of the ramp. A closeup of the comparison in this region is shown in Fig. 16. The temperatures seen in the laminar calculation are more in agreement with the experiment than the turbulent calculation. The laminar calculation also shows velocity vectors aligned more parallel to the wall than the turbulent calculation, again more similar to the experimental result. The discrepancy in the turbulent calculation may be due to unreasonable turbulent viscosities predicted by the Baldwin-Lomax model used in this region. This model was originally developed for simple flows over flat plates and is somewhat inapplicable to this highly three-dimensional separated region. Improved two-equation models, such as the k-ϵ model, may be better suited to these complex three-dimensional flows.

Conclusions

The PLIIF technique for measuring time-averaged pressure, temperature, velocity, and injectant mole fraction has been applied to a study of swept ramp injection into a supersonic flowfield. Within the range of thermodynamic conditions present in the flowfield studied, the technique's accuracy is estimated to be 4% for pressure, temperature, and velocity and 3% for injectant mole fraction. Agreement with a CFD calculation using the SPARK three-dimensional Navier-Stokes solver is within about 5%, except in specific regions of the flowfield. The following are specific conclusions drawn from the experimental and numerical comparison:

1) Separation due to shock-wave/boundary-layer interaction at the top wall is captured well by the calculation, but the
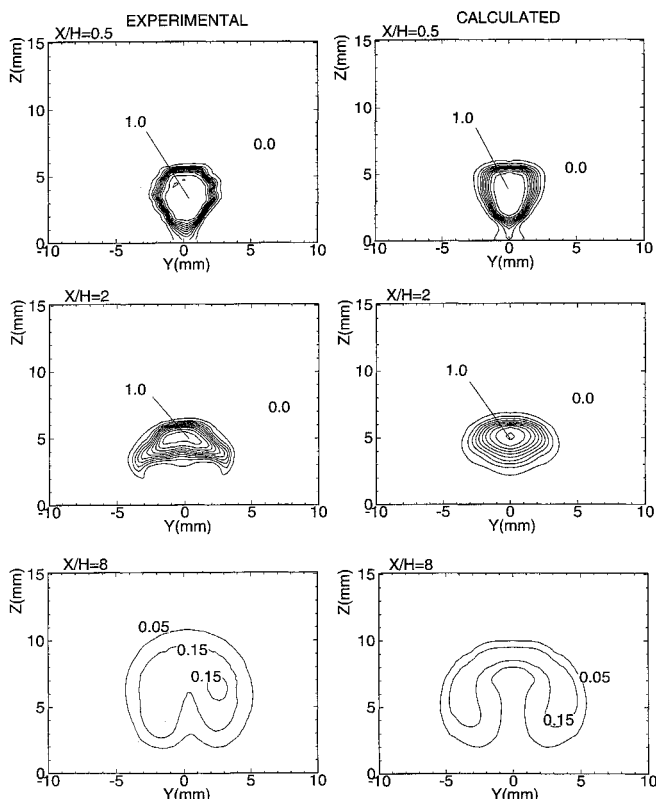

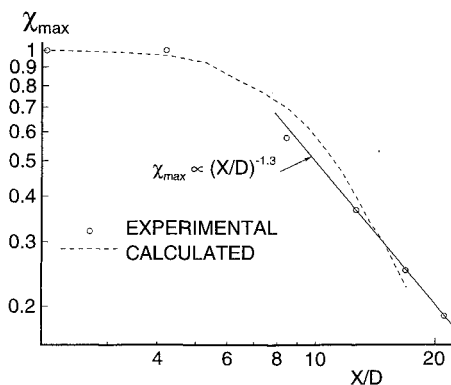Fig. 14 Crossflow plane injectant mole fraction distributions.

Fig. 15 Decay of the maximum injectant mole fraction vs streamwise distance (nondimensionalized by injector orifice throat diameter).

effect of treating the sidewalls with slip conditions may have an important effect on the shock structure and location of sidewall reflections. Asymmetry observed in the experimental results may be due to, or amplified by, the shock-induced separated regions.

2) The measured strength of the ramp-generated vortices is greater than in the calculation, having the effect of greater turning and mixing of the jet plume in the experiment. Numerical viscosity, due to insufficient grid resolution, damps the strong pressure and velocity gradients in the core of the calculated vortices.

3) The rate of decay of the maximum injectant mole fraction with streamwise distance is greater for the present ramp injection scheme than for previously measured transverse injection schemes. The higher decay exponent (-1.3 vs -0.8) is due to stronger streamwise vortices formed by the ramp.

4) The temperature and velocity field in the recirculation region at the base of the ramp are better predicted by a laminar than a turbulent calculation.

Acknowledgments

References

[1]Hartfield, R. J., Jr., Hollo, S. D., and McDaniel, J. C., "Experimental Investigation of a Supersonic Swept Ramp Injector Using Laser-Induced Iodine Fluorescence," *Journal of Propulsion and Power,* Vol. 10, No. 1, 1994, pp. 129–135.

[2]Riggins, D. W., Mekkes, G. L., McClinton, C. R., and Drummond, J. P., "A Numerical Study of Mixing Enhancement in a Supersonic Combustor," AIAA Paper 90-0203, Jan. 1990.

[3]Waitz, I. A., Marble, F. E., and Zukoski, E. E., "An Investigation of a Contoured Wall Injector for Hypervelocity Mixing Augmentation," *AIAA Journal,* Vol. 31, No. 6, 1993, pp. 1014–1021.

[4]Riggins, D. W., and McClinton, C. R., "Analysis of Losses in Supersonic Mixing and Reacting Flows," AIAA Paper 91-2266, June 1991.

[5]Eklund, D. R., Fletcher, D. G., Hartfield, R. J., Jr., McDaniel, J. C., Northam, G. B., Dancey, C. L., and Wang, J. A., "Computational/Experimental Investigation of Staged Injection into a Mach 2 Flow," *AIAA Journal,* Vol. 32, No. 5, 1994, pp. 907–916.

[6]Rapagnani, N. L., and Davis, S. J., "Laser-Induced Iodine Fluorescence Measurements in a Chemical Laser Flowfield," *AIAA Journal,* Vol. 17, No. 12, 1979, pp. 1402–1404.

[7]Fletcher, D. G., "Spatially-Resolved, Nonintrusive Measurements in a Nonreacting Scramjet Combustor Using Laser-Induced Iodine Fluorescence," Ph.D. Dissertation, Dept. of Mechanical and Aerospace Engineering, Univ. of Virginia, Charlottesville, VA, Jan. 1989.

[8]Hartfield, R. J., "Planar Measurement of Flow Field Parameters in Nonreacting Supersonic Flows with Laser-Induced Iodine Fluorescence," Ph.D. Dissertation, Dept. of Mechanical and Aerospace Engineering, Univ. of Virginia, Charlottesville, VA, May 1991.

[9]Hartfield, R. J., Jr., Hollo, S. D., and McDaniel, J. C., "A Unified Planar Measurement Technique for Compressible Flows Using Laser-Induced Iodine Fluorescence," *AIAA Journal,* Vol. 31, No. 3, 1993, pp. 483–490.

[10]McDaniel, J. C., Fletcher, D., Hartfield, R., and Hollo, S. D., "Staged Transverse Injection into Mach 2 Flow Behind a Rearward-Facing Step: A 3-D Compressible Test Case for Hypersonic Combustor Code Validation," AIAA Paper 91-5071, Dec. 1991.

[11]Hartfield, R. J., Abbitt, J. D., and McDaniel, J. C., "Injectant Mole Fraction Imaging in Compressible Mixing Flows Using Planar Laser-Induced Iodine Fluorescence," *Optics Letters,* Vol. 14, No. 16, 1989, pp. 850–852.

[12]Donohue, J. M., Victor, K. G., and McDaniel, J. C., "Computer-Controlled Multi-Parameter Mapping of 3D Compressible Flowfields Using Planar Laser-Induced Iodine Fluorescence," AIAA Paper 93-0048, Jan. 1993.

[13]Drummond, J. P., "A Two Dimensional Numerical Simulation of a Supersonic, Chemically Reacting Mixing Layer," NASA TM-4055, Dec. 1988.

[14]Carpenter M. H., "Three-Dimensional Computations of Cross-Flow Injection and Combustion in a Supersonic Flow," AIAA Paper 89-1870, June 1989.

[15]Eklund, D. R., and Northam, G. B., "A Numerical Study of the Effects of Geometry on the Performance of a Supersonic Combustor," AIAA Paper 92-0625, Jan. 1992.

[16]Hollo, S. D., McDaniel, J. C., and Hartfield, R. J., Jr., "Quantitative Investigation of Compressible Mixing: Staged Transverse Injection into Mach 2 Flow," *AIAA Journal,* Vol. 32, No. 3, 1994, pp. 528–534.